Fluid-structure interactions for the air blast loading of elastomer-coated concrete

C. Fallon[a], G.J. McShane[a,*]

[a]*Department of Engineering, University of Cambridge, Trumpington Street, Cambridge CB2 1PZ, UK*

Abstract

The fluid-structure interaction (FSI) effect experienced by an elastomer-coated concrete slab subjected to blast loading in air is studied numerically. The aim is to establish whether a flexible coating alters blast-structure interactions and whether this can explain the apparent blast mitigating capability of this retrofit solution as reported in published experimental investigations. Numerical models for a typical concrete and spray-on elastomer coating are established and a Coupled Eulerian-Lagrangian (CEL) model is employed to predict the air blast response. A 1D FSI analysis suggests that the elastomer coating increases the peak compressive stress in the concrete during short timescale pressure wave interactions. But the effect on the total imparted momentum is small, across a range of target mass and blast intensity. However, due to momentum sharing, the impulse imparted to the concrete plate is reduced in the coated configuration. By extending the analysis into 2D, it is found that the displacement of a concrete slab is marginally reduced when coated on either the blast-receiving or non-blast-receiving face. Thus, it is postulated that the elastomer contributes a small, beneficial mechanical effect. Finally, the need for a fully coupled (CEL) approach to model the blast-structure interaction is interrogated. For a wide range of cases, the results suggest that using a purely Lagrangian approach, in which a pressure-time history is directly applied to the structure (thereby neglecting full representation of FSI effects), is sufficient to capture the deflection behaviour of coated concrete plates. However, it is shown that the significance of the error associated with this simplification depends on the blast intensity and slab geometry under consideration.

*Corresponding author

Email addresses: cf335@cam.ac.uk (C. Fallon), gjm31@cam.ac.uk (G.J. McShane)

Keywords: blast, elastomer, concrete, FSI

1. Introduction

Increasing concerns related to terrorist activity have shaped global agendas towards the protection and resilience of critical buildings and infrastructure. Despite the current attention focused on the need to design for enhanced blast resilience in the built-environment, it is accepted that there is still a great deal yet to be understood regarding the effects of blast on structures and how best to mitigate them.

Blast loading itself is a complex phenomenon. It is a transient, dynamic event which presents many modelling challenges, analytically and numerically. The simplest approximation of a typical blast wave is the exponential time-dependence of the imparted pressure given by Eq. 1, (see, for example, Kambouchev *et al.* [1]):

$$p(t) = p_s e^{-\frac{t}{t_i}} \qquad 0 \leq t \leq \infty \tag{1}$$

where p_s is the peak overpressure and t_i is the decay time. Thus, the incident impulse:

$$I_i = \int_0^\infty p(t)dt = p_s t_i \tag{2}$$

While new buildings can be designed with higher threat levels in mind, existing structures remain vulnerable if the threat level changes. Retrofitting buildings and infrastructure for enhanced blast resistance is one approach to solving this problem. One particular retrofit solution that has gained attention in recent years is the use of a spray-on elastomer coating. Early experiments on masonry structures yielded encouraging results regarding the elastomer's ability to contain blast debris [2, 3]. Further work on elastomer application to steel plates has suggested that it is also capable of significantly reducing peak deflections due to dynamic loading [4–6]. However, there is some debate in the literature regarding the optimum coating location *i.e.* whether it is more beneficial to coat the blast-receiving or non-blast-receiving face. Indeed, some researchers have reported that the coating can have detrimental effects if applied to the load-receiving face of a steel substrate [4, 5].

Comparatively little work has focused on spray-on elastomers applied to a concrete substrate, despite concrete representing a significant proportion of the aging, vulnerable infrastructure in today's built environment that could benefit from such a retrofit solution. In one study by Raman *et al.* [7], a numerical analysis is used to investigate the performance of a polyurea-coated, reinforced concrete slab. Results indicated that polyurea coatings can significantly contribute to controlling panel displacement, and deflection reductions of more than 40% were reported. However, the question remains as to what mechanism is responsible for this apparent enhancement in blast resistance: is the elastomer effect a purely mechanical one, or does the application of an elastomer coating to a concrete slab introduce a fluid-structure interaction (FSI) effect?

There are various examples in the literature whereby the introduction of a compliant layer gives rise to beneficial FSI effects. For example, this phenomenon has been exploited for blast mitigation in the case of sandwich panels subject to underwater blast loading [8, 9]. However, it is not clear whether FSI can explain the apparent enhanced air blast resistance observed for concrete panels coated with a spray-on elastomer coating.

G.I. Taylor [10] performed one of the first investigations to explore FSI effects for the case of underwater explosions. He analysed the interaction between a 1D blast wave and a rigid plate and proposed that the FSI effect was governed by a single, non-dimensional parameter. Further, he was able to quantify the relative impulse transmitted to the plate, as a function of this non-dimensional parameter.

The 2006 work of Kambouchev *et al.* [1] expands upon the work of Taylor [10] to account for non-linear compressibility effects during FSI, with a focus on the air blast loading of structures. They consider the case of a free-standing plate, of arbitrary mass, impacted by a planar blast wave, propagating in a compressible medium. An expression (Eq. 3) is postulated for the relative transmitted impulse, I_p/I_i.

$$\frac{I_p}{I_i} = \gamma_R \left(\frac{C_R f_R}{\gamma_R}\right)^{\beta_s/(1+\beta_s)} \beta_s^{\beta_s/(1-\beta_s)} \tag{3}$$

where I_p is the transmitted impulse to the plate, I_i is the incident blast impulse and C_R, γ_R and f_R are parameters derived in [1].

The compressibility is encapsulated in the revised FSI parameter, β_s that is now dependent on blast intensity parameters.

$$\beta_s = \frac{t_i \rho_s U_s}{\rho_p h_p} \tag{4}$$

where h_p is the plate thickness and ρ_p is the density of the plate. ρ_s is the density of the compressed blast medium and U_s is the shock propagation speed, each defined by Rankine-Hugoniot relations in [1]. Similarly to Taylor [10], this parameter represents the relative time scales of the blast wave duration, t_i and of the fluid-structure interaction, t_s^*.

Throughout this investigation, we will employ finite element analysis using the commercial code, Abaqus/Explicit [11]. The paper is structured as follows. First, a fully coupled Eulerian-Lagrangian (CEL) finite element model is developed. Appropriate constitutive models for concrete and an elastomer coating are attained. For coated configurations, the present study focuses on the case of perfect bonding between the concrete and elastomer. We begin with a high resolution 1D investigation to study the stress wave interactions between the air/polymer/concrete interfaces over very short time scales. This allows us to consider the various non-linear effects in the air (compressibility), polymer (hyperelasticity, viscoelasticity) and the quasi-brittle substrate, concrete. We follow this with longer duration 1D calculations to interrogate the effect of these non-linearities on the total impulse transmission. For a practical range of concrete and coating thicknesses, the influence of coating on the imparted momentum to each layer is assessed. We extend our investigation to the 2D response to examine any interplay between FSI effects (acting over short timescales) and any longer timescale mechanical benefit that might arise from the elastomer coating, for both a low and high intensity blast. It emerges that the function of the elastomer depends on the response regime of the slab and thus motivates a need for further interrogation of performance sensitivity to the coating, substrate and blast parameters. In order to facilitate this, we quantitatively assess the suitability of simplified numerical modelling strategies, that would enable such a study at reduced computational cost.

2. Numerical model development

2.1. Concrete constitutive model

The Concrete Damaged Plasticity (CDP) model in Abaqus/Explicit [11] is chosen for the concrete material model. The model does not track individual macrocracks but rather considers the concrete as a continuum which exhibits isotropic, damaged elasticity and isotropic, pressure-dependent plasticity. Pressure dependent damage is prescribed via compressive crushing and tensile cracking responses.

The model parameters are summarised here, with further details provided in Appendix A. To implement this model, the compressive behaviour is defined in terms of the uniaxial compressive stress, σ_c *vs.* inelastic strain, $\tilde{\epsilon}_c^{in}$ according to the empirical relationships set out in the CEB-FIP Model Code [12]. The tensile response is based on the relationship proposed by Hordijk [14] for the uniaxial tensile stress, σ_t in terms of cracking displacement, u_t^{ck}. Damage is incorporated through the use of compressive and tensile damage parameters, d_c and d_t which quantify the degradation of elastic stiffness and can take values between zero (undamaged material) and one (fully damaged material). The compressive and tensile damage parameters are defined as a function of inelastic strain, $\tilde{\epsilon}_c^{in}$ and cracking displacement, u_t^{ck}, respectively, according to the relationship proposed by Birtel and Mark [15]. To complete the definition, the CDP model employs the yield function proposed by Lubliner *et al.* [16] and includes the modifications suggested by Lee and Fenves [17]. Further, a non-associated plastic flow rule is assumed whereby the flow potential takes the form of the Drucker-Prager hyperbolic function. We assume a concrete compressive strength of 39.5 MPa and tensile strength, 4.2 MPa. The undamaged elastic modulus is 28.3 GPa, the Poisson's ratio is 0.2 and the density is $2550\,\mathrm{kg\,m^{-3}}$.

In this investigation, we opt to omit strain rate dependence in the constitutive response of the substrate. There is currently a lack of published data on the strain rate dependence of the full suite of constitutive parameters in the CDP model. This constitutive assumption might affect the model fidelity, in terms of reproducing specific experimental results (for which a more detailed representation of the blast loading conditions would also be required). However, within the scope of this investigation, it provides an adequate model for studying the fundamentals of FSI effects for a quasi-brittle substrate, representative of concrete. [1]

[1] Additional calculations were performed in Appendix A.2 to check, nonetheless, that the predictive quality of the model is reasonable, for dynamic structural response in the regimes of interest.

2.2. Elastomer constitutive model

To help develop a representative material model for the elastomer, we take as a reference material a sample of commercially available, spray application polyurea/polyurethane hybrid. The sample coatings were sprayed to a thickness of around $3-5\,\mathrm{mm}$ (precise control of thickness is not possible) onto an untreated steel plate and then peeled off. Characterisation tests on the coating were performed in tension, compression and shear, as follows.

Uniaxial tension tests were performed on dogbone specimens, machined from this sheet, shown in Fig. 1. The geometry was based on the ASTM D182 standard [23], but modified to ease manufacture and enable testing on a servo-hydraulic materials testing rig.

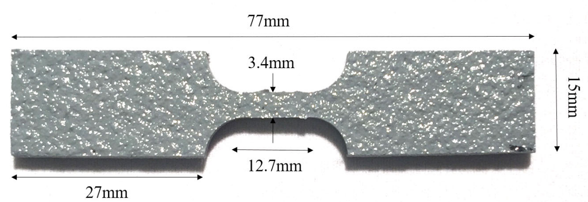

Figure 1: Tensile specimen used to characterise the polyurea/polyurethane hybrid spray-on elastomer. The thickness of the specimen is 3.5 mm, though this varied between specimens.

An Instron screw-driven materials testing machine was used to perform tensile testing at low to moderate nominal strain rates, in the range $10^{-3}-10^{0}\,\mathrm{s}^{-1}$. Higher nominal strain rates, in the range $10^{0}-10^{2}\,\mathrm{s}^{-1}$ were achieved using a servo-hydraulic materials testing machine. The resulting nominal stress-nominal strain results up to failure are presented in Fig. 2. It is observed that the response is non-linear and strain rate dependent. A substantial increase in failure stress with increasing strain rate is noted, though failure strains do not show considerable strain rate dependency.

Next, a constitutive model is developed for the polymer on the basis of the tensile data. This will subsequently be validated against characterisation tests performed in compression and shear. Rather than trying to match precisely the response of a particular coating, the aim is to achieve a material model representative of a realistic elastomer coating to allow subsequent interrogation of the key phenomena at play. First, a hyperelastic constitutive relationship is fitted to the uniaxial tensile response up to a nominal strain $\epsilon = 1$, using the data obtained at a nominal strain rate, $\dot{\epsilon} = 10^{-3}\,\mathrm{s}^{-1}$ (assumed to be the long term

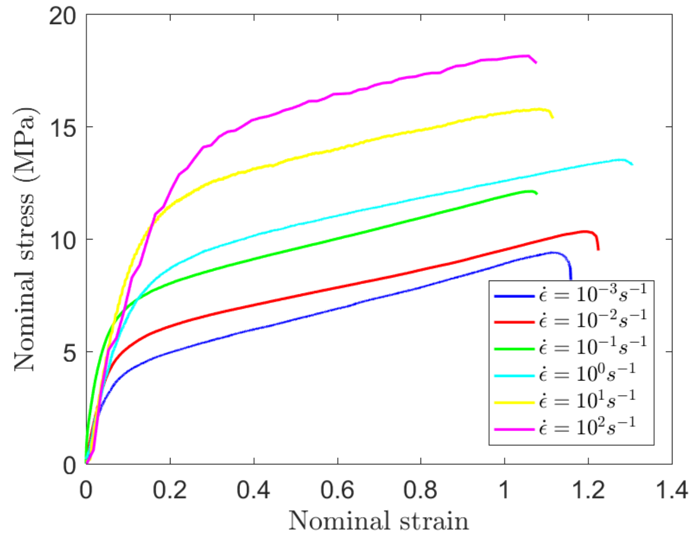

Figure 2: Uniaxial tensile results at various strain rates, $\dot{\epsilon}$ for the elastomer sample.

i.e. relaxed response). A Yeoh strain energy potential is found to give the best fit and its formulation is presented in Appendix A.3. A nearly incompressible variant of the model was selected, corresponding to a Poisson's ratio of $\nu = 0.475$ (a small degree of compressibility was required for numerical reasons). The density was chosen as $\rho_e = 1.1\,\mathrm{Mg/m^3}$. A Prony series is used in conjunction with this hyperelastic model to provide a viscoelastic model suitable for a finite strain analysis (see [11]). The Prony series parameters are presented in Appendix A.3 (obtained from Table 3.4 in [24]).

In order to validate the material model, first the ability of the viscoelastic model to predict the experimentally measured strain rate dependence in uniaxial tension was tested. Abaqus/Explicit was used to simulate a uniaxial tension test at strain rates of up to $10^2\,\mathrm{s}^{-1}$, which is indicative of the blast regime [25]. The resulting nominal stress-nominal strain plot is compared with that obtained experimentally in Fig. 3a. No failure criterion was included in the numerical model so the failure stresses and strains are not comparable. In order to isolate the effect of the Prony series on the shape of the stress-strain curve at higher strain rates, an additional result is shown (labelled inviscid) for which the Prony series is removed, but the hyperelastic strain energy potential is re-fitted to the higher strain rate data measured at $10^2\,\mathrm{s}^{-1}$.

Reasonable agreement is observed between the numerical model and the experiment in

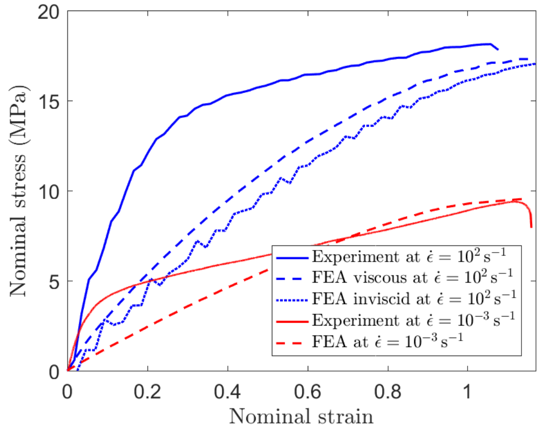

(a) Uniaxial tension

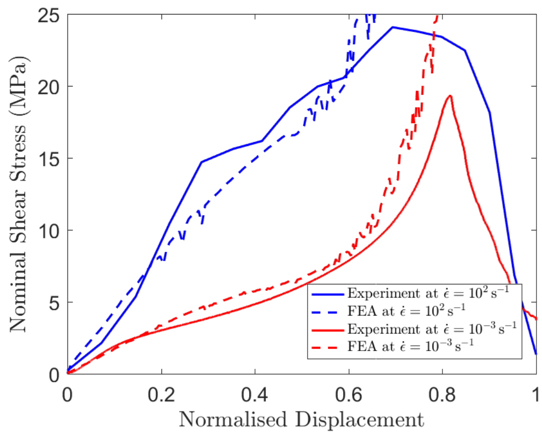

(b) Shear punch

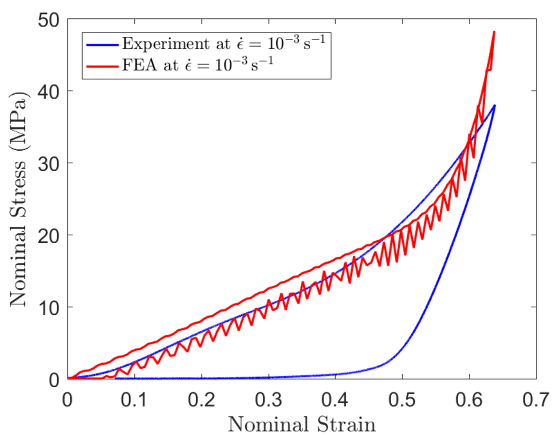

(c) Compression

Figure 3: Comparison between experimental results and those obtained via the numerical model. Uniaxial tension and shear punch results are compared for strain rates, $10^{-3}\,\mathrm{s}^{-1}$ and $\dot{\epsilon} = 10^2\,\mathrm{s}^{-1}$. Compression data is presented for $\dot{\epsilon} = 10^{-3}\,\mathrm{s}^{-1}$. Two numerical models are considered — an inviscid model based on data measured at $\dot{\epsilon} = 10^2\,\mathrm{s}^{-1}$ and a viscous model based on data measured at $\dot{\epsilon} = 10^{-3}\,\mathrm{s}^{-1}$.

terms of the strain rate dependence and the stresses at larger strains. However, the model underpredicts the initial modulus, not capturing precisely the shape of the measured tensile response curve.

To test the material model under alternative stress states, shear punch experiments were performed using the rig illustrated in Fig. 4a. The polymer specimen (thickness $h_e \approx 3.5\,\mathrm{mm}$) was clamped between a pair of steel plates, and loaded through a hole in the centre of the plates by a circular cylindrical punch (diameter $d = 8\,\mathrm{mm}$), driven by a servo-hydraulic test machine. The test machine cross-head velocities spanned several orders of magnitude to simulate the strain rates expected during a blast loading event.

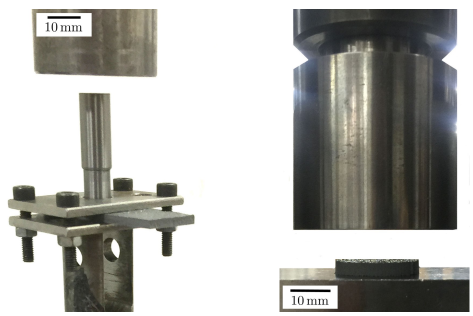

(a) Shear punch (b) Compression

Figure 4: Rigs used for the shear punch and compression disc experiments. For shear punch, the specimen is sandwiched between steel plates of thickness 3 mm and impacted by a rigid punch of diameter 8 mm. For compression, 25.9 mm diameter samples are compressed by a platen 40 mm in diameter.

Abaqus/Explicit was then used to simulate the shear punch experimental test at the highest cross-head velocity achievable by the servo-hydraulic machine, $\dot{x} = 900\,\mathrm{mm/s}$, indicative of a nominal strain rate, $\dot{\epsilon} = 10^2\,\mathrm{s}^{-1}$. A plot of the nominal shear stress at the perimeter of the punch (given by $P/\pi d h_e$, where P is the punch force) *vs.* normalised displacement (given by δ_p/h_e, where δ_p is the punch displacement) is compared with the experimental results in Fig. 3b. Once again, no failure criterion was included in the numerical model. Again, the viscoelastic model captures the strain rate dependence well. The model also predicts the initial stiffness better for shear loading, compared to uniaxial tension. To further validate the model, compression of thin discs was performed at $\dot{\epsilon} = 10^{-3}\,\mathrm{s}^{-1}$ on an Instron screw-driven materials testing machine as illustrated in Fig. 4b. Results are compared with numerical predictions in Fig. 3c. Loading and unloading is shown. Although the model fails to capture the observed hysteresis, very good agreement is achieved for the loading portion of the curve.

Throughout this study, we will proceed with this viscoelastic material model in the numerical analysis of the spray-on elastomer. Although the strain energy potential fails to capture accurately the shape of the tensile response, the model does capture well the strain rate dependence, and the responses in compression and shear.

2.3. Coupled Eulerian-Lagrangian (CEL) model

In order to capture the fully coupled air blast response, a Coupled Eulerian-Lagrangian (CEL) model was built in Abaqus/Explicit. A Lagrangian domain is used for the target structure, with the Eulerian domain capturing the air. In order to validate the model, a one-dimensional test case was developed. It simulates the behaviour of a rigid plate (Lagrangian domain), placed in an air column (Eulerian domain), impacted by a blast wave. The model is illustrated in Fig. 5 where point A corresponds to the point at which the blast pulse enters the air column and point B corresponds to the point of first impingement by the blast wave on the rigid target. The CEL model and its validation are summarised here, with further details provided in Appendix B.

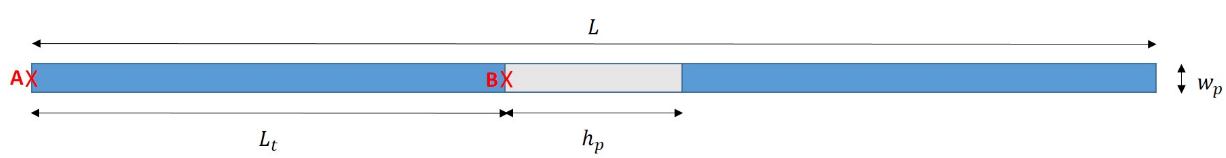

Figure 5: A schematic illustration of the 1D CEL model in Abaqus/Explicit.

It is assumed that the air can be modelled as an ideal gas [26] with the model parameters presented in Table B.6. The blast pulse is generated by specifying a velocity-time boundary condition to the end of the column at A. The velocity is specified in the direction AB, to generate a compressive pressure pulse. After having determined a finite element mesh density that can adequately resolve the propagating shock front, an iterative process can be employed to determine what velocity-time history is necessary at point A, to achieve the desired pressure-time history at point B. Iteration is necessary as the wave shape changes during propagation. This iterative process is similar to that presented by Chen *et al.* [28] using the Rankine-Hugoniot equations to relate particle velocity to peak overpressure.

To validate the CEL technique, in terms of its ability to resolve FSI effects, we compare calculated results for the relative transmitted impulse with Kambouchev *et al.*'s [1] analytical expression for a free-standing, rigid plate of arbitrary mass, given by Eq. 3. Very good agreement is found between the two FSI predictions (see Fig. B.17). This gives a strong indication that the CEL approach in Abaqus/Explicit is capable of accurately analysing fluid-structure interaction problems across the range of blast intensities of interest. The results indicate that for the case of low β_s values, the relative transmitted impulse becomes insensitive to β_s. This suggests that there is negligible fluid-structure interaction in this regime, as there is little plate movement during its interaction with the blast. Conversely, for lighter plates, as β_s increases, there is a significant reduction in relative transmitted impulse to the plate relative to this heavy plate limit. This can be attributed to motion of the plate during the period of blast loading.

3. 1D wave interaction study

We begin our study by first examining in 1D the details of pressure wave propagation through the air/polymer/concrete interfaces. We examine the very short time scale response, using a high resolution numerical calculation, with the objective of determining whether the presence of a thin elastomer coating can serve to distort the blast wave. A number of non-linear effects are at play, such as air compressibility, concrete damaged elasticity and plasticity, and hyperelasticity and viscoelasticity in the polymer. Thus, the effect of the polymer can not necessarily be determined *a priori*, by analytical means.

We implement the 1D CEL model described above, replacing the rigid plate with a deformable, Concrete Damaged Plasticity part of density, $\rho_p = 2550\,\mathrm{kg\,m^{-3}}$ and compressive strength, $\sigma_{cu} = 39.5\,\mathrm{MPa}$. A concrete plate depth, $h_p = 100\,\mathrm{mm}$ is considered. On the basis of a mesh sensitivity study, it is determined that the shock front width (which is of the order of 20 mm in the concrete, and 4 mm in the air column) is adequately resolved with a mesh size of 1 mm in all material layers. 3D stress (C3D8) elements are used for the concrete and polymer while 3D Eulerian (EC3D8R) elements are chosen for the air column. All elements are constrained to permit only 1D deformations. A 5 mm thick elastomer coating is considered, positioned on the blast-receiving face, and we assume a perfect bond between the concrete and polymer, simulated by tying all degrees of freedom at the interface. We examine the intermediate blast intensity case considered by Kambouchev *et al.* [1] corresponding to a peak overpressure of $p_s/p_0 = 3.29$. As described in Appendix B, we achieved $p_s/p_0 = 3.34$, $I_i = 698\,\mathrm{Pa\,s}$ and $t_i = 2.0\,\mathrm{ms}$ in our CEL model.

Figure 6 illustrates the spatial variation in the compressive stress at various times after impingement on the blast receiving face, for three configurations: concrete alone, concrete coated with a hyperelastic polymer on its blast-receiving face and concrete coated with a visco-hyperelastic polymer on its blast-receiving face. We note that in the latter case, when unloading occurs, the FE model predictions may lose fidelity, as the elastomer constitutive model does not capture the hysteresis of the polymer accurately. (However, as discussed subsequently, the key longer timescale effects appear to be insensitive to this.)

We observe that the addition of a polymer layer causes significant distortion to the wave front due to both the non-linear elasticity and viscoelasticity in the polymer. Higher peak stresses are observed in the concrete as a consequence of the coating. It is therefore necessary to examine the longer timescale response, including the total impulse transmission and the development of any plasticity or damage in the substrate, which is discussed next.

4. 1D air blast response of a concrete part

Before proceeding to study the influence of an elastomer coating, the longer time scale air blast response of uncoated concrete is first considered. The aims, for a realistic range of areal mass and blast parameters, are; (i) to determine the regime of FSI response relative to the heavy and light plate limits identified by [1] and (ii) to identify any FSI effects attributable to concrete elasticity, plasticity or damage. In this section, the scope is restricted to the 1D FSI response. The 2D response of a slab will be described subsequently.

For a fixed concrete density of $\rho_p = 2550\,\mathrm{kg\,m^{-3}}$, four different plate thicknesses were considered: $h_p = 25\,\mathrm{mm}$, $50\,\mathrm{mm}$, $75\,\mathrm{mm}$ and $100\,\mathrm{mm}$. This corresponds to areal densities of 63.75 , 127.5, 191.25 and $255\,\mathrm{kg\,m^{-2}}$, respectively. Two different blast intensity cases were examined; the first is the intermediate intensity case considered by Kambouchev *et al.* [1] corresponding to a peak overpressure of $p_s/p_0 = 3.29$. As described in Appendix B, we achieved $p_s/p_0 = 3.34$, $I_i = 698\,\mathrm{Pa\,s}$ and $t_i = 2.0\,\mathrm{ms}$ in our CEL model.

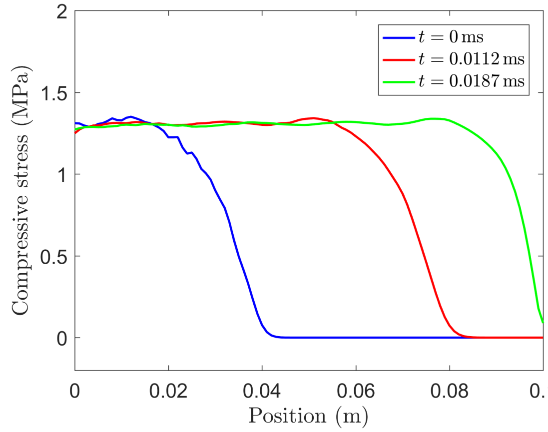

(a) Concrete only

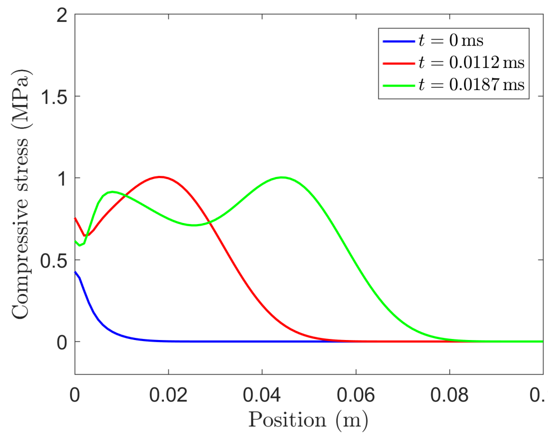

(b) Concrete coated with hyperelastic polymer

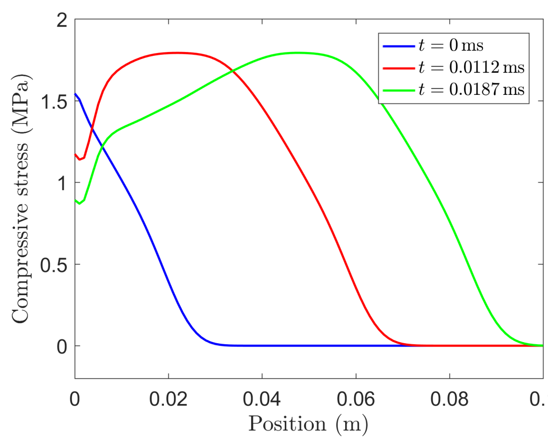

(c) Concrete coated with visco-hyperelastic polymer

Figure 6: Stress profile in the concrete plate at three different time steps: $t = 0\,\mathrm{ms}$, $t = 0.0112\,\mathrm{ms}$ and $t = 0.0187\,\mathrm{ms}$ where t is the time after first impingement of the blast wave on the target structure. Plotted for three configurations: a) concrete only, b) concrete coated with a hyperelastic polymer on its blast-receiving face and c) concrete coated with a visco-hyperelastic polymer on its blast-receiving face.

Using the empirical relationships proposed by Kinney and Graham [29], the blast parameters corresponding to examples of realistic threats in the built environment are presented in Table 1. The second blast case considered in our study corresponds to 20 kg of TNT at a stand-off distance of 15 m, indicative of a "suitcase bomb". β_s values were calculated for each case and are summarised in Table 2.

Table 1: Examples of realistic blast threats where the peak overpressure, p_s and incident impulse, I_i are calculated using Kinney and Graham's empirical relationships [29].

Threat [30]	kg of TNT	Stand-off (m)	p_s (kPa)	I_i (Pa s)
Pipe bomb	3	15	9.4	19
Suitcase bomb	20	15	24	34
Car bomb	300	15	158	80
Truck bomb	5000	15	1320	120

Table 2: Summary of the β_s values obtained using Eq. 4 for each concrete depth, h_p considered, for both blast intensity cases.

	β_s	
h_p (mm)	Case 1, $p_s/p_0 = 3.34$	Case 2, $p_s/p_0 = 0.24$
25	0.068	0.012
50	0.034	0.006
75	0.023	0.004
100	0.017	0.003

The model set-up is as described in Appendix B except that the rigid plate is replaced with a deformable part assigned the Concrete Damaged Plasticity material model with a compressive strength, $\sigma_{cu} = 39.5\,\mathrm{M\,Pa}$. The mesh consists of 8-node linear elements (C3D8 in Abaqus notation) of side length 5 mm, chosen on the basis of a mesh sensitivity study. The relative transmitted impulse, I_p/I_i to the concrete plates is compared with Kambouchev *et al.*'s theoretical expression for a rigid plate, Eq. 3 [1] as well as the numerical predictions for a rigid plate of equivalent β_s. The results are presented in Fig. 7.

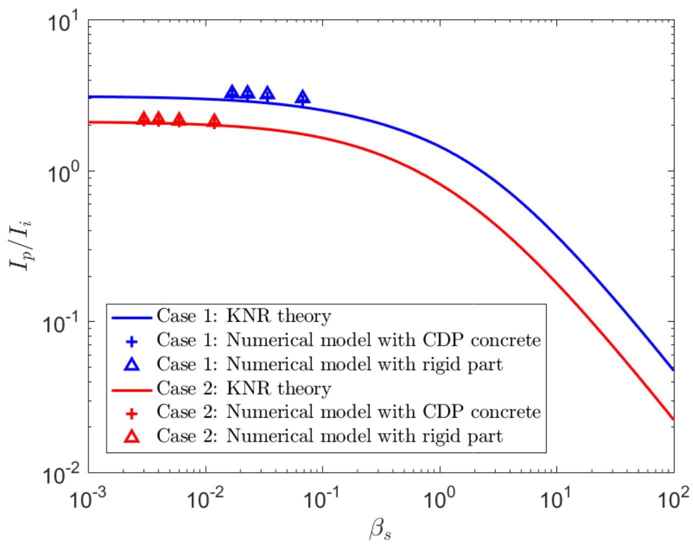

(a) Log-log plot

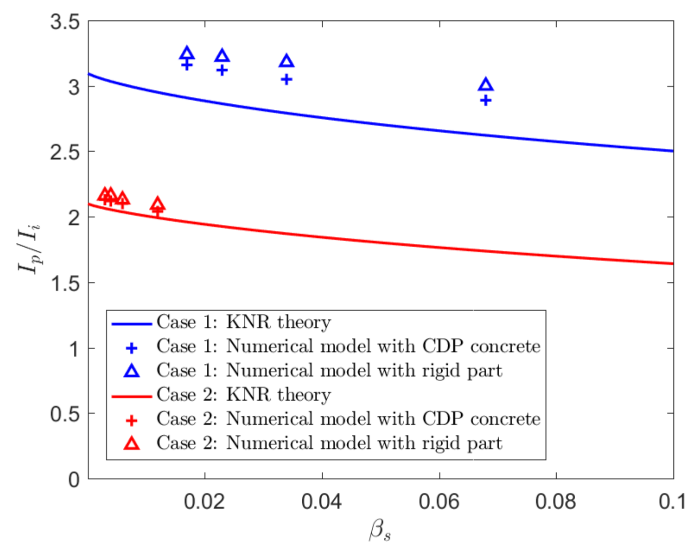

(b) Non-log plot of region of interest

Figure 7: Comparing numerical predictions with Kambouchev *et al.*'s (KNR) theory [1] for a rigid plate and concrete plates of depth: 25 mm, 50 mm, 75 mm and 100 mm. Case 1 refers to the medium intensity blast referred to in KNR's work where $p_s/p_o = 3.34$ and $I_i = 698\,\mathrm{Pa\,s}$. Case 2 refers to our "suitcase bomb" reference blast indicative of 20 kg of TNT at a stand-off distance of 15 m; $p_s/p_o = 0.24$ and $I_i = 34\,\mathrm{Pa\,s}$.

Firstly, the concrete plates appear to lie on the "heavy plate" plateau of Kambouchev *et al.*'s theoretical expression. It would appear that for realistic concrete density and slab depths, the calculated β_s values are relatively low. In this region, I_p is relatively insensitive to β_s *i.e.* to the blast intensity and to the plate mass per unit area. On closer inspection (Fig. 7b), we observe that the FSI response of the concrete is close to that of a rigid plate of the same mass. This can be explained as follows. First, the model predicted no plasticity or damage occurring in the concrete during either load case. So, the plate remained elastic throughout FSI. Secondly, it can be shown that the transit time of an elastic wave through the plate is short compared to the duration of loading, and so the influence of stress wave propagation on FSI would be negligible. The elastic wave speed in concrete is, $c_d = \sqrt{E_0/\rho_p}$. For the largest concrete plate depth considered, $h_p = 100\,\mathrm{mm}$, the transit time for the elastic wave is given by;

$$t_T = \frac{h_p}{c_d} = \frac{h_p}{\sqrt{E/\rho_p}} = 30\,\mu\mathrm{s} \tag{5}$$

Considering a blast intensity corresponding to $p_s/p_o = 3.34$, the propagation time, t_T is much smaller than the decay time of the incident blast wave, $t_i = 2\,\mathrm{ms}$.

Incidentally, we also note that Kambouchev *et al.*'s [1] theory gives a slightly lower prediction of the transmitted impulse in this regime compared to the numerical calculations.

5. 1D air blast response of an elastomer-coated concrete part

In the final phase of the 1D investigation, an elastomer layer is applied to the concrete plate to assess whether it enables an FSI effect that might offer a contribution to protection.

A 5 mm thick elastomer layer is modelled as a deformable part, and meshed with 5 mm 3D stress (C3D8) elements. A mesh refinement investigation is performed on the 1D model (and for the 2D model, discussed subsequently). It is found that the overall response is relatively mesh insensitive, provided the Eulerian, air mesh density is matched to that of the Lagrangian concrete and elastomer coating. Boundary conditions are prescribed to ensure plane strain conditions throughout. In this study, we assume a perfect bond between the concrete and polymer, simulated by tying all degrees of freedom at the interface. Three plate configurations are analysed, illustrated in Fig. 8. The reference case is an uncoated concrete plate at a stand-off, $s = 3\,\mathrm{m}$. Next, a 5 mm elastomer layer is applied to either the blast-receiving or non-blast-receiving face of a CDP plate. In both cases, the stand-off, $s = 3\,\mathrm{m}$ measured to the blast-receiving face of the target is held constant. Thus, the shape of the incident pressure pulse by the time it has reached the blast-receiving face is the same in all cases. Figure 9 presents the calculated total transmitted impulse for plates of different mass per unit area for two blast intensities. Four plate thicknesses are considered — 25 mm, 50 mm, 75 mm and 100 mm. This corresponds to a mass per unit area of, 63.75, 127.5, 191.25 and 255 $\mathrm{kgm^{-2}}$ for the uncoated concrete, and 69.32, 133.07, 196.82 and 260.57 $\mathrm{kgm^{-2}}$ for the coated cases. The coatings therefore increase the mass of the target by 8.7%, 4.4%, 2.9% and 2.2%, respectively. In each configuration, the impulse imparted to the complete target plate (concrete plus elastomer, if present) is plotted, as well as the impulse transmitted to the concrete layer alone, when in its coated configuration. Also, comparison is made in each case with the response of a rigid plate of the same mass.

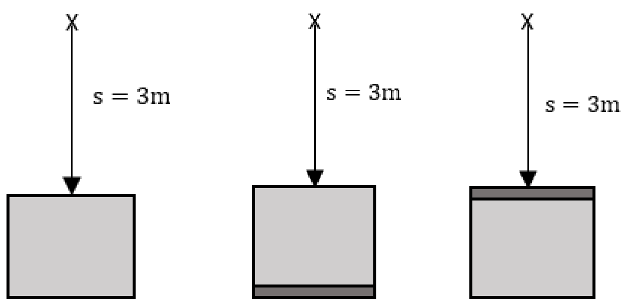

(a) Case *i* (b) Case *ii* (c) Case *iii*

Figure 8: Schematic illustrating the stand-off distance, s for analysis of both coated and uncoated cases.

5.1. Discussion

Considering the results in Fig. 9, four key observations are made:

- Firstly, it is found that the concrete elasticity (compliance and thus, impedance) has the effect of reducing the imparted momentum, compared to a rigid plate of the same mass.

- It appears that the imparted impulse to the composite configuration (coated concrete) is insensitive to the coating location, thus suggesting that coated concrete behaves as

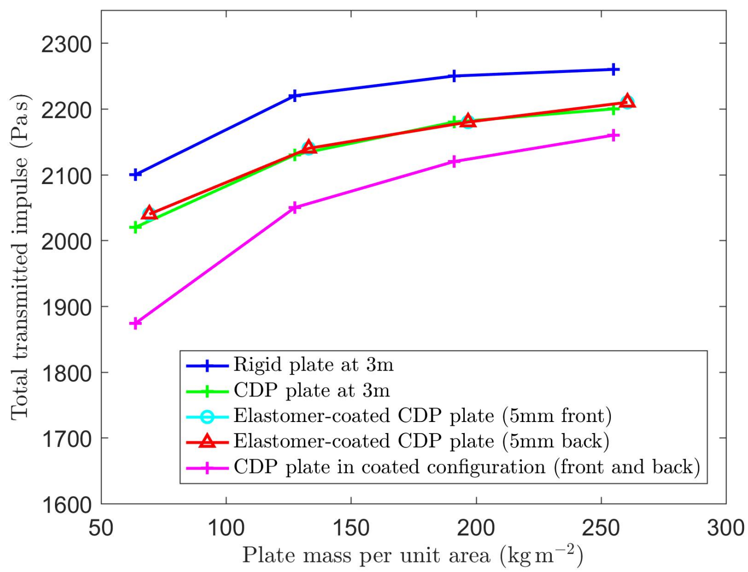

(a) Blast Case 1: $p_s/p_o = 3.34$ and $I_i = 698\,\mathrm{Pa\,s}$

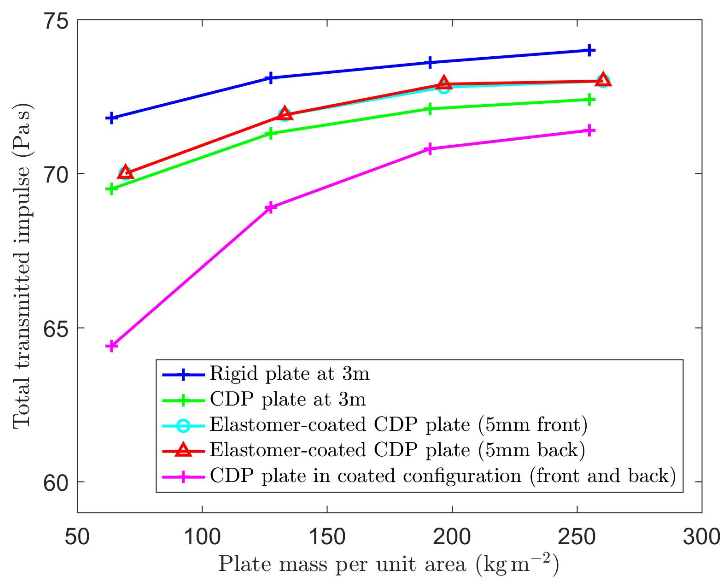

(b) Blast Case 2: $p_s/p_o = 0.24$ and $I_i = 34\,\mathrm{Pa\,s}$.

Figure 9: A plot showing how total transmitted impulse varies with plate mass per unit area for four plate configurations: uncoated rigid and CDP plates of depth: 25 mm, 50 mm, 75 mm and 100 mm, and for CDP plates of these depths, coated with 5 mm elastomer on either the blast-receiving or the non-blast-receiving face.

a monolithic plate, of mass equal to the mass of the concrete plus the mass of the polymer, from the perspective of FSI.

- The coated concrete composite acquires slightly more momentum than a monolithic concrete plate *of the same mass*. However, this effect is negligible and is likely due to a change in effective compliance of the plate. Figure 6 illustrated that during the short timescale response, the effect of adding a viscoelastic polymer layer led to substantial wave distortion and an increase in peak compressive stress in the concrete. Here, we show that while this has a small effect on the transmitted impulse to the coated configuration (pushing it towards that of a rigid plate), it is apparent that the longer timescale response is relatively insensitive to the short timescale pulse distortion effects.

- Although the composite plate acquires slightly more momentum than the uncoated concrete plate, the *concrete* layer in the composite configuration acquires less. This is because each layer acquires a fraction of the total imparted momentum in proportion to the mass fraction of that layer (assuming perfect bonding *i.e.* both concrete and elastomer acquire the same velocity). The effect is most significant for the lightest plate tested ($63.75\,\mathrm{kgm^{-2}}$) where there is an $8\,\%$ reduction in transmitted impulse to the concrete. This diminishes as the plate mass increases. For the $255\,\mathrm{kgm^{-2}}$ plate, the reduction is $2\,\%$. Any mechanical benefit of this *momentum sharing* between the concrete and polymer layers on critical slab deflections and failure mechanisms remains to be determined.

6. 2D coupled Eulerian-Lagrangian model

In this section, we extend the analysis to consider the 2D response of coated and uncoated concrete slabs to explore any interplay between the short timescale FSI effects and any mechanical benefit offered by the coating during slab flexure. The 2D model geometry is illustrated in Fig. 10. We consider a concrete slab of dimensions typical of structural elements: 50 mm deep, with a span of 1 m. The boundary conditions at the end of slab are illustrated in Fig. 10. The end faces of the slab are fully constrained, with all degrees of freedom set to zero. To avoid unrealistic stress concentrations at the boundary, a degree of boundary compliance is introduced: a 50 mm length at the end of the slab is placed between rigid, frictionless surfaces, which terminate with a radius of curvature of 90 mm. The slab is placed in a 6 m long air column, at a target distance, $L_t = 3$ m. In all cases, a planar blast wave is modelled. A half-model only is simulated, using symmetry boundary conditions at mid-span. The slab is modelled in 2D plane strain.

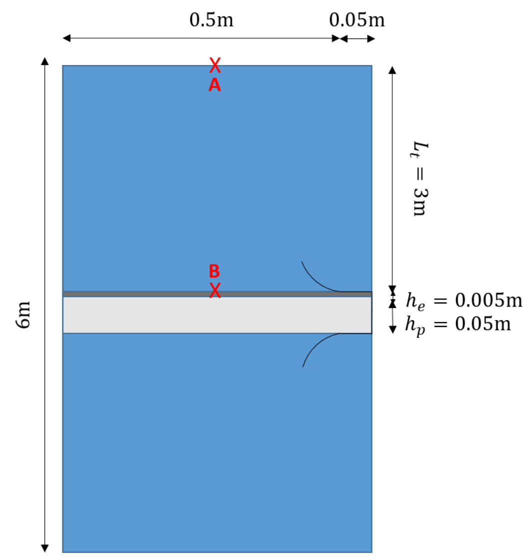

Figure 10: A schematic illustration of the 2D CEL 1/2-model in Abaqus/Explicit. A CDP part of depth, $h_p = 0.05$ m and width 0.55 m is placed in a 6 m long air column, at a target distance, $L_t = 3$ m. The CDP part is coated with elastomer of depth, $h_e = 5$ mm. Point A corresponds to the inflow of the air column and point B corresponds to the point of first impingement by the blast wave on the elastomer-coated concrete. The diagram is not to scale.

As before, two blast intensities are considered and for each case, the mid-span displacement-time response is compared for an uncoated concrete slab, a concrete slab coated with a 5 mm elastomer on the blast-receiving face and a concrete slab coated with a 5 mm elastomer on the non-blast-receiving face. The results are presented in Fig. 11. Two distinct response regimes are observed for the two loading cases.

For the higher blast impulse, Case 1, total failure of the slab occurs early in its motion. This occurs at a time of around 0.0063 s, as indicated by the dashed line in Fig. 11a. Failure occurs by extensive tensile cracking and significant damage near the support region. The effect of the polymer coating in this regime is to reduce the mid-span deflection at a given time, before failure. This reduction is $\sim 5\%$ for coating on either the blast-receiving or

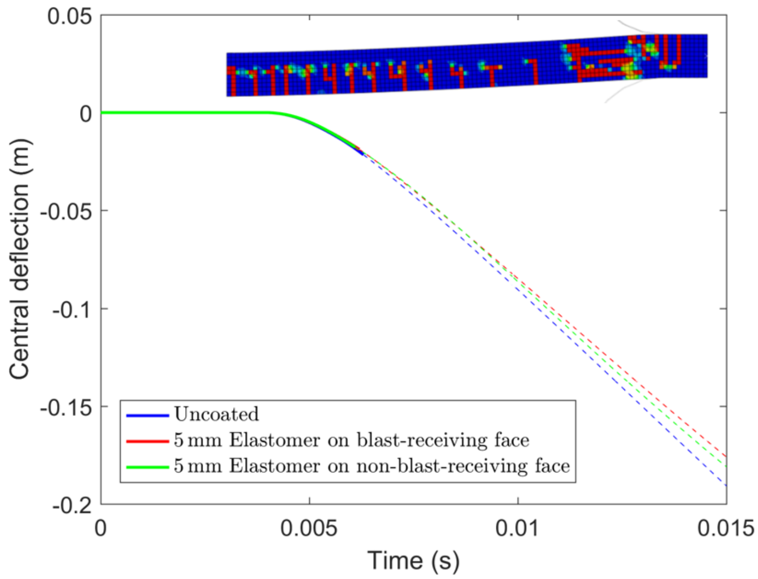

(a) Blast Case 1: $p_s/p_o = 3.34$ and $I_i = 698\,\mathrm{Pa\,s}$

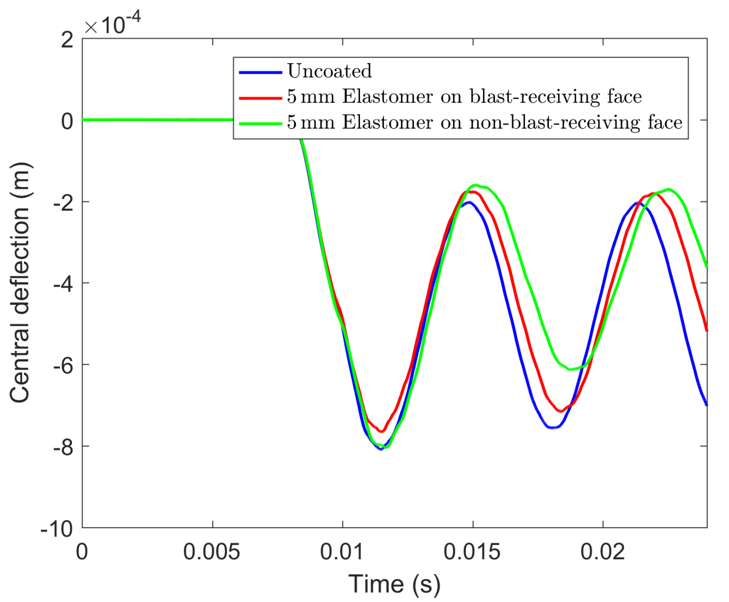

(b) Blast Case 2: $p_s/p_o = 0.24$ and $I_i = 34\,\mathrm{Pa\,s}$

Figure 11: Central deflection (m) *vs.* time (s) for the slab geometry illustrated in Fig. 10 for two blast intensity cases. Results are compared for an uncoated concrete slab, a concrete slab with a 5 mm elastomer coating applied to the blast-receiving face and a concrete slab with a 5 mm elastomer coating applied to the non-blast-receiving face. Inset to a) is a snapshot at a step time of 0.0063 s of the damaged uncoated slab for Blast Case 1.

non-blast-receiving face. However, the coating does not have a significant effect on altering the mechanism or onset of failure for this loading intensity.

For the lower blast impulse, Case 2, the slab responds by elastic-plastic bending. The deflections are small, with a peak predicted deflection of 0.81 mm (1.6% of the slab thickness), before elastic oscillations about a permanent deflection of around 0.48 mm for the uncoated case. The polymer coatings serve to reduce permanent slab deflections by 5% and 18% when located on the blast-receiving and non-blast-receiving faces, respectively. Although the coating appears to have no significant effect on the total transmitted impulse to the target, it appears to contribute an additional mechanical resistance to bending.

In summary, the regime of response was not affected by the coating for these load cases, though we do show a protective benefit in terms of reduced deflections. The load cases here represent lower and upper bounds on realistic blast impulses in a structural protection context. However, there are a wide range of other possible regimes of response at intermediate impulse levels, for other pressure-impulse combinations, and for other slab geometries. The role of the polymer coating across this full regime map requires further analysis.

6.1. Coupled vs. decoupled response

In order to tackle the problem of identifying the full range of response regimes for coated structural elements, it is useful to consider the necessity of a fully coupled Eulerian-Lagrangian analysis. This adds significantly to the computational cost, but may not be justified if the coatings do not induce a strong FSI effect. In this section, the scope for simplifying the load case is assessed.

Three simplified load cases are considered, progressively decoupling the loading from the slab response, for comparison with the fully coupled CEL simulations.

(i) A pressure-time history, $p_1(t)$ is applied directly to the blast-receiving face of the slab, in a purely Lagrangian analysis (*i.e.* with no air domain). However, the applied loading is obtained by outputting the pressure-time history calculated at the slab-air interface (at point B in Fig. 10) in the coupled simulation. This is the pressure *felt* by the slab in a fully coupled FSI analysis.

(ii) A pressure-time history, $p_2(t)$ is again applied directly to the blast-receiving face of the slab in a Lagrangian analysis. However, this time, the applied pressure-time history is obtained by applying a pressure reflection coefficient factor, C_R (defined in [1]) to the *free-field* incident overpressure, p_s measured at point B in Fig. 10. We assume that the decay time of the applied pressure-time history remains the same as the incident value, t_i.

The value of C_R is taken to be the heavy plate limit (*i.e.* $\beta_s = 0$ [1]). This gives $C_R = 3.9$ for the higher intensity blast case considered ($p_s/p_o = 3.34$) and $C_R = 2.2$ for the lower intensity blast case considered ($p_s/p_o = 0.24$). (Note that in the acoustic limit, C_R would be equal to 2). Thus, we remove FSI effects (because the heavy plate limit for C_R is used), but retain a loading timescale.

(iii) Lastly, we consider impulsive loading, in which an initial velocity is imparted uniformly to the slab, again in a fully Lagrangian simulation. Here, the initial velocity is equal to the imparted impulse, I_p (obtained by integrating the $p_2(t)$ profile) divided by the mass per unit area of the slab, $m = \rho_p h_p + \rho_e h_e$ [31]. Thus, we remove both the FSI effect and the timescale of loading.

Results for the slab geometry illustrated in Fig. 10, are presented in Fig. 12 for the high intensity blast ($p_s/p_o = 3.34$) and Fig. 13 for the low intensity blast ($p_s/p_o = 0.24$). The results suggest that the slab's deflection-time history can be accurately represented using a simpler load case, though the accuracy depends on the blast impulse. For both blast impulses, we find that direct application of $p_1(t)$ or $p_2(t)$ matches well the response of the fully coupled analysis. Impulsive loading is reasonably accurate for the higher blast impulse case, apart from at short timescales (of the order of t_i). However, it significantly over-predicts the slab deflections for the lower blast impulse case.

7. Conclusions

Elastomer coatings have been previously reported as an effective solution for protecting structural components against blast loading. However, to date, the mechanisms responsible have not been clearly identified. In this investigation, we present the first detailed study of

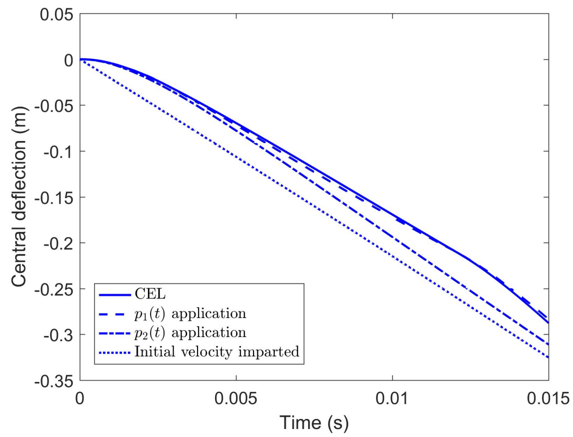

(a) Uncoated

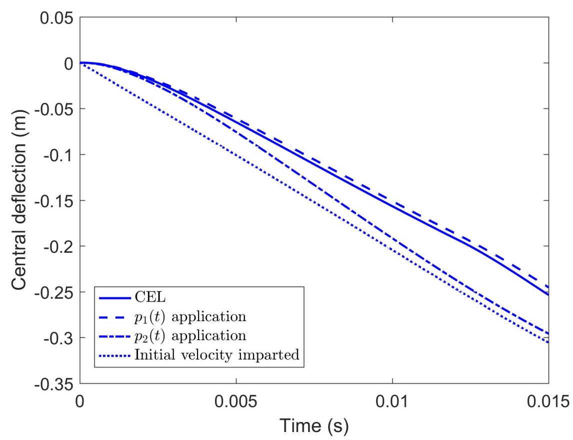

(b) Coated on blast-receiving face

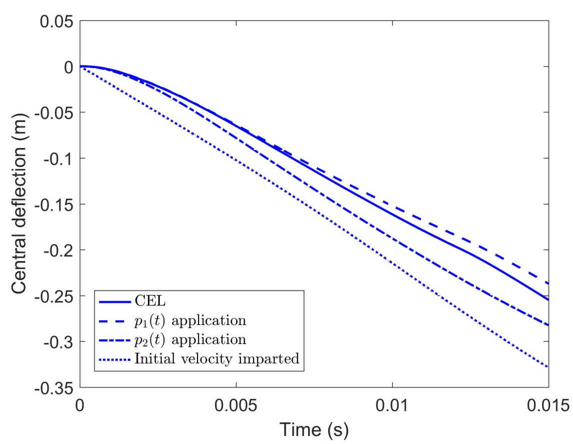

(c) Coated on non-blast-receiving face

Figure 12: Central deflection (m) *vs.* time (s) for the slab geometry illustrated in Fig. 10 for Blast Case 1: $p_s/p_o = 3.34$ and $I_i = 698\,\mathrm{Pa\,s}$ ($t_i = 0.00205\,\mathrm{s}$). Results are compared for a Coupled Eulerian-Lagrangian (CEL) model, a purely Lagrangian model with loading applied by direct application of a pressure-time history, $p_1(t)$, $p_2(t)$ and for a purely Lagrangian model with impulsive loading applied by imparting an initial velocity. Note, total failure of the slab occurs early in its motion, c. 0.0063 s.

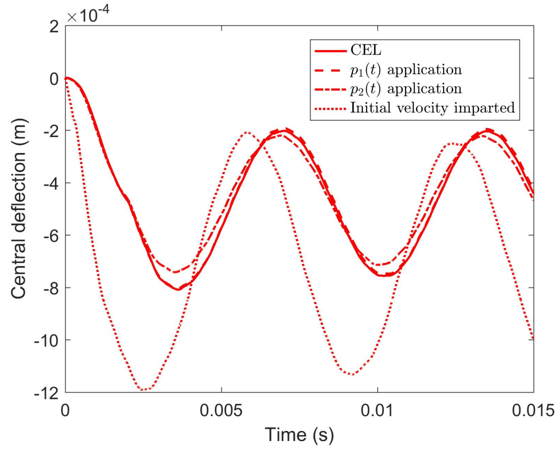

(a) Uncoated

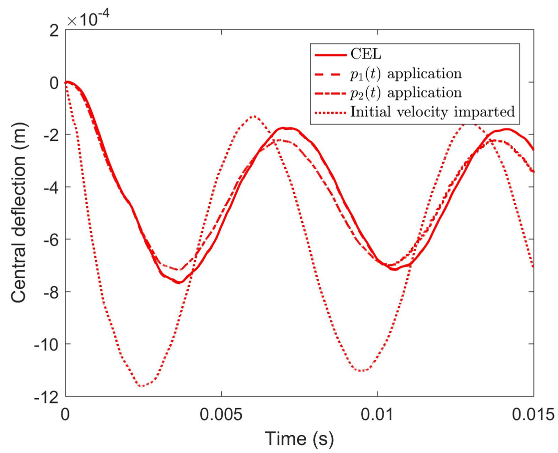

(b) Coated on blast-receiving face

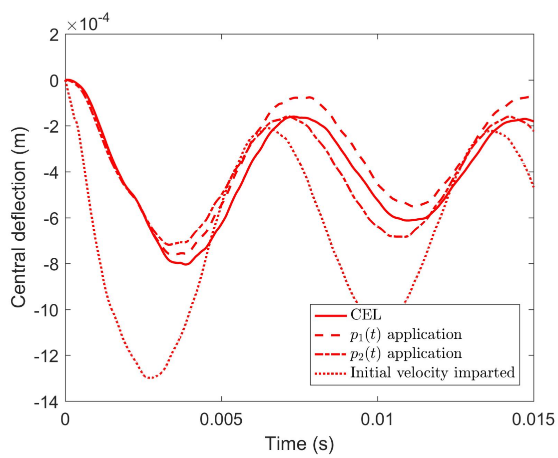

(c) Coated on non-blast-receiving face

Figure 13: Central deflection (m) *vs.* time (s) for the slab geometry illustrated in Fig. 10 for Blast Case 2: $p_s/p_o = 0.24$ and $I_i = 34\,\mathrm{Pa\,s}$ ($t_i = 0.0014\,\mathrm{s}$). Results are compared for a Coupled Eulerian-Lagrangian (CEL) model, a purely Lagrangian model with loading applied by direct application of a pressure-time history, $p_1(t)$, $p_2(t)$ and for a purely Lagrangian model with impulsive loading applied by imparting an initial velocity.

one candidate mechanism for concrete structural elements: fluid-structure interaction (FSI) effects during blast loading.

- Representative constitutive models for concrete and a spray-on elastomer are developed using a combination of published data and our own characterisation experiments.

- A coupled Eulerian-Lagrangian finite element model is verified as an effective tool for studying the fully coupled FSI response for air-blast loading. Comparison with Kambouchev *et al.*'s theory [1] over a wide range of the non-dimensional FSI parameter, β_s verifies the model fidelity.

- A high resolution, short timescale, 1D stress wave interaction study shows that the presence of an elastomer coating significantly influences the transient stress state in the concrete during initial wave propagation through the layered structure. The non-linear elasticity of the polymer reduces the peak compressive stress, but introducing viscoelasticity results in a net increase.

- The longer timescale, 1D FSI response of coated and uncoated concrete is then assessed, to identify the effect of coating on the total imparted momentum. It is found that, for practical concrete thicknesses and blast impulses, the transmitted impulse for both coated and uncoated plates approaches the heavy plate limit as defined by Kambouchev *et al.*'s theory [1]. In this regime of β_s, the imparted impulse is insensitive to the target mass.

- It is found that the imparted momentum is more sensitive to the elasticity of the concrete than to the target mass. Replacing a rigid target with a concrete target reduces the imparted momentum, for a given target mass. But the effect is small ($\sim 3\%$).

- It is also found that coating (on either face) has a negligible influence on the total imparted momentum. However, due to momentum sharing, the impulse imparted to the concrete plate is reduced in the coated configuration (by up to $\sim 8\%$ for the lightest plates).

- For blast impulses representative of a small improvised explosive device, a small additional mechanical resistance to bending is identified with the addition of the coating. The net effect is that peak deflections are largely unchanged, though permanent deflections are reduced by between $5 - 18\%$, depending on the polymer location.

- For a much higher blast impulse, the slab undergoes extensive cracking, and failure at the support. The coating provides a small reduction in slab deflection, but does not prevent slab failure.

- Finally, it is concluded that a partially decoupled Lagrangian analysis, maintaining the timescales of loading but assuming the heavy plate limit of imparted impulse, provides a reasonable substitute for the fully coupled FSI calculation. This result will facilitate future investigations of the dynamic mechanical benefit offered by the coatings across a wider range of blast pressure-impulse regimes.

8. Acknowledgements

The authors are grateful to the George and Lillian Schiff Foundation of the University of Cambridge for financial support.

Appendix A. Further details on material constitutive modelling

Appendix A.1. Concrete

Empirical relationships were employed to generate the curves required by Abaqus/Explicit for the complete definition of the Concrete Damaged Plasticity (CDP) material model. The approach taken is similar to that presented in [13].

Appendix A.1.1. Defining compressive behaviour

To define the uniaxial compressive stress, σ_c *vs.* inelastic strain, $\tilde{\epsilon}_c^{in}$ curve; the empirical relationships proposed by the 1990 CEB-FIP Model Code [12] are used. Figure A.14 illustrates a typical uniaxial compressive stress-strain curve for concrete where the first part of the curve, for $|\epsilon_c| < |\epsilon_{c,lim}|$ can be described using Eq. A.1 and the descending branch can be described using Eq. A.2 [12].

$$\sigma_c = -\frac{\frac{E_0}{E_s}\frac{\epsilon_c}{\epsilon_{c1}} - (\frac{\epsilon_c}{\epsilon_{c1}})^2}{1 + (\frac{E_0}{E_s} - 2)\frac{\epsilon_c}{\epsilon_{c1}}}\sigma_{cu} \qquad \text{for} \qquad |\epsilon_c| < |\epsilon_{c,lim}| \tag{A.1}$$

$$\sigma_c = -\left[\left(\frac{1}{\frac{\epsilon_{c,lim}}{\epsilon_{c1}}}\zeta - \frac{2}{(\frac{\epsilon_{c,lim}}{\epsilon_{c1}})^2}\right)\left(\frac{\epsilon_c}{\epsilon_{c1}}\right)^2 + \left(\frac{4}{\frac{\epsilon_{c,lim}}{\epsilon_{c1}}} - \zeta\right)\frac{\epsilon_c}{\epsilon_{c1}}\right]^{-1}\sigma_{cu} \qquad \text{for} \qquad |\epsilon_c| > |\epsilon_{c,lim}| \tag{A.2}$$

$$\text{where} \qquad \zeta = \frac{4\left[\left(\frac{\epsilon_{c,lim}}{\epsilon_{c1}}\right)^2\left(\frac{E_0}{E_s} - 2\right) + 2\frac{\epsilon_{c,lim}}{\epsilon_{c1}} - \frac{E_0}{E_s}\right]}{\left[\frac{\epsilon_{c,lim}}{\epsilon_{c1}}\left(\frac{E_0}{E_s} - 2\right) + 1\right]^2} \tag{A.3}$$

$$\text{and} \qquad E_0 = E_{c0}\left[\frac{\sigma_{cu}}{\sigma_{cu0}}\right]^{\frac{1}{3}} \tag{A.4}$$

where

σ_c is the compressive stress in MPa;

E_0 is the initial tangent modulus in MPa;

$E_{c0} = 2.15 \times 10^4\,\text{MPa}$;

σ_{cu} is the peak compressive stress in MPa;

$\sigma_{cu0} = 10\,\text{MPa}$;

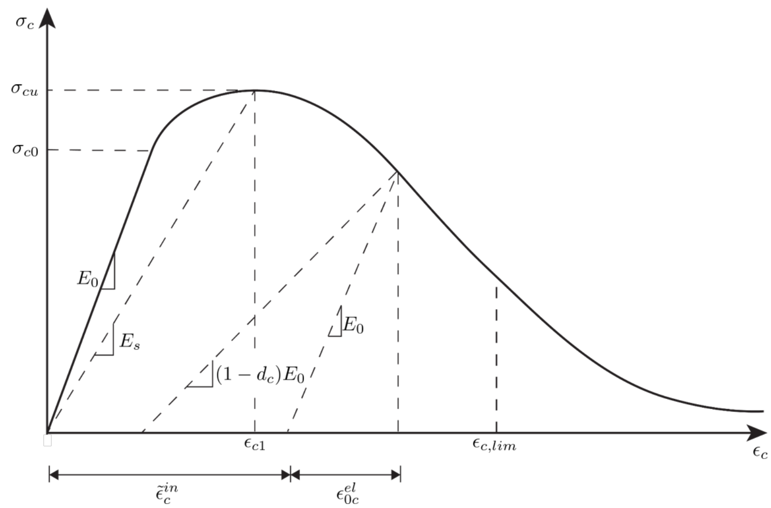

(a) Compressive behaviour

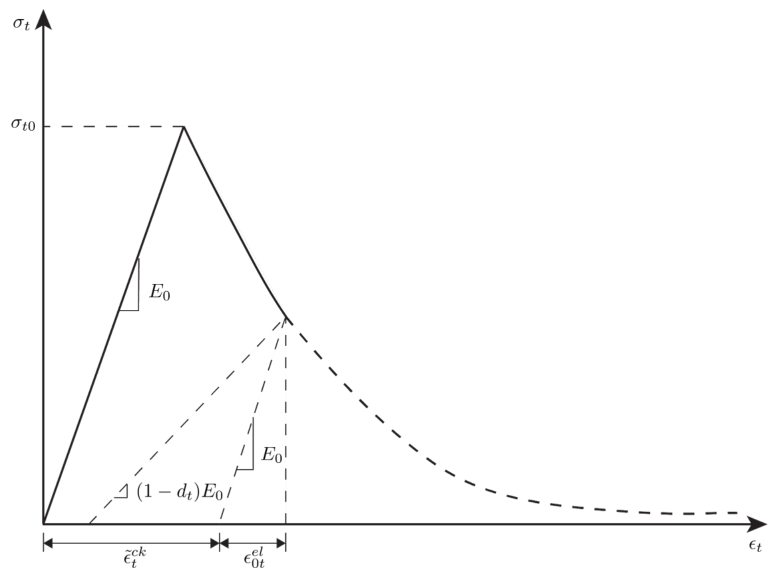

(b) Tensile behaviour

Figure A.14: Compressive and tensile behaviour definitions for the ABAQUS/Explicit Concrete Damaged Plasticity model (adapted from [11]). Parameters are defined in the text.

ϵ_c is the compressive strain;

$\epsilon_{c1} = 0.0022$ is the strain corresponding to the peak compressive stress;

$E_s = \sigma_{cu}/0.0022$ is the secant modulus from the origin to the peak compressive stress in MPa;

$\epsilon_{c,lim}$ limits the applicability of Eq. A.1 and is calculated using Eq. A.5.

$$\frac{\epsilon_{c,lim}}{\epsilon_{c1}} = \frac{1}{2}\left(\frac{1}{2}\frac{E_0}{E_s}+1\right) + \left[\frac{1}{4}\left(\frac{1}{2}\frac{E_0}{E_s}+1\right)^2 - \frac{1}{2}\right]^{1/2} \tag{A.5}$$

Appendix A.1.2. Defining tensile behaviour

There are two methods permitted by ABAQUS for defining the post-failure branch of the uniaxial, tensile stress-strain curve. Typically, tensile stress, σ_t is given as a function of cracking strain, $\tilde{\epsilon}_t^{ck}$ which is defined as the total tensile strain, ϵ_t minus the elastic strain corresponding to the undamaged material, ϵ_{0t}^{el}. This definition is illustrated in Fig. A.14 where $\epsilon_{0t}^{el} = \sigma_t/E_0$.

However, as noted in the ABAQUS User's Manual [11], in cases where the concrete has little or no reinforcement, choosing to define the post-failure behaviour in terms of cracking strain can introduce unreasonable mesh sensitivity. The Manual [11] suggests that it would be more reliable to specify post-failure tensile stress, σ_t as a function of cracking displacement, u_t^{ck}, based on the 1976 work of Hillerborg [18]. To achieve this, the relationship proposed by Hordijk [14] in his work on concrete fatigue is employed, given by Eq. A.6.

$$\frac{\sigma_t}{\sigma_{t0}} = \left[1 + \left(c_1\frac{u_t^{ck}}{u_t^{crit}}\right)^3\right]\exp\left(-c_2\frac{u_t^{ck}}{u_t^{crit}}\right) - \frac{u_t^{ck}}{u_t^{crit}}\left(1+c_1^3\right)\exp(-c_2) \tag{A.6}$$

$$\text{where} \qquad u_t^{crit} = 7\,\frac{G_F}{\sigma_{t0}} \quad \text{mm} \tag{A.7}$$

$$\text{and} \qquad G_F = G_{F0}\left(\frac{\sigma_{cu}}{\sigma_{cu0}}\right)^{0.7} \quad \text{N/mm} \tag{A.8}$$

where

u_t^{crit} is the critical crack opening displacement, beyond which the tensile stress is zero. This is calculated according to Eq. A.7 which is taken from the CEB-FIP code [12] and is based on a concrete with medium aggregate size of approximately 16 mm;

$c_1 = 3$ and $c_2 = 6.93$ are constants determined by Hordijk [14] based on deformation-controlled uniaxial tests on normal-weight concrete;

σ_{to} is the tensile strength in MPa;

G_F is the tensile fracture energy of concrete in opening mode in N/mm;

G_{F0} is the base value of fracture energy which depends on the maximum aggregate size. Assuming a maximum aggregate size of 16 mm, the CEB-FIP code [12] recommends a value of $G_{F0} = 0.03\,\mathrm{N/mm}$.

Appendix A.1.3. Defining damage parameters

The CDP model in ABAQUS/Explicit allows the user to define compressive and tensile damage parameters, d_c and d_t that quantify how the concrete elastic stiffness becomes degraded when unloaded from the softening branch of the uniaxial curves.

Compressive damage.

For the compressive damage case, Birtel and Mark [15] propose the following relationship between the damage parameter, d_c and the compressive inelastic strain, $\tilde{\epsilon}_c^{in}$:

$$d_c = \frac{\tilde{\epsilon}_c^{in}\,(1 - b_c)}{\tilde{\epsilon}_c^{in}\,(1 - b_c) + \frac{\sigma_c}{E_o}} \qquad 0 \leq d_c \leq 1 \tag{A.9}$$

Through comparison with experimental data, Birtel and Mark determined that the best fit was achieved using $b_c = 0.7$ in Eq. A.9 [15]. Thus, a curve can be obtained for d_c as a function of $\tilde{\epsilon}_c^{in}$.

Tensile damage.

An equation of the same form as Eq. A.9 [15] can also be used to define a curve for the tensile damage parameter, d_t in terms of cracking displacement, u_t^{ck} and fitting parameter, b_t. Best fit with experimental data was achieved for $b_t = 0.1$ [15].

Appendix A.1.4. Yield surface and flow rule

The CDP model in ABAQUS/Explicit employs the yield function proposed by Lubliner *et al.* [16] and includes the modifications suggested by Lee and Fenves [17]. The shape of the yield surface is determined by K_c, a user-defined ratio based on the second stress invariants [11].

The flow rule specifies the relationship between the yield surface and the uniaxial stress-strain relationships. Non-associated plastic flow is assumed by the CDP model where the flow potential takes the form of the Drucker-Prager hyperbolic function. Further details on the yield surface and flow rule can be found in the Abaqus User's Manual [11].

Table A.3 presents the parameters required to fully define the yield surface and flow rule. Values used for ϵ, f_{b0}/f_{c0}, K_c and the viscosity parameter are the default parameters suggested by ABAQUS [11]. The dilation angle, ψ is chosen to be 36° [19].

Table A.3: User-defined parameters required to define the yield surface and flow rule in the Concrete Damaged Plasticity model in ABAQUS/Explicit.

Dilation angle, ψ	Eccentricity, ϵ	f_{b0}/f_{c0}	K_c	viscosity parameter
36°	0.1	1.16	0.667	0

Appendix A.2. Validating the Concrete Damaged Plasticity model

To validate the developed CDP model's predictive capabilities, model predictions are compared with two sets of published experimental results on the blast testing of reinforced concrete slabs [20, 21]. Loading was implemented via the CONWEP option in ABAQUS/Explicit [22], specifying the mass of TNT explosive charge and stand-off distances to match the experiments. While this load application does not capture the full details of the FSI or close-in blast effects, it enables broad assessment of the model to first order under realistic conditions. The concrete and reinforcing steel material properties and geometries are modelled to match those reported in the literature reference cases [20, 21].

The numerical predictions of cracking and spall patterns were qualitatively compared with experimental observations for a concrete slab subjected to 0.31 kg of TNT at a stand-off of 0.4 m [20]. Figures A.15 and A.16 show that the model is capable of predicting well the characteristic crack patterns for both the blast-receiving and non-blast-receiving faces.

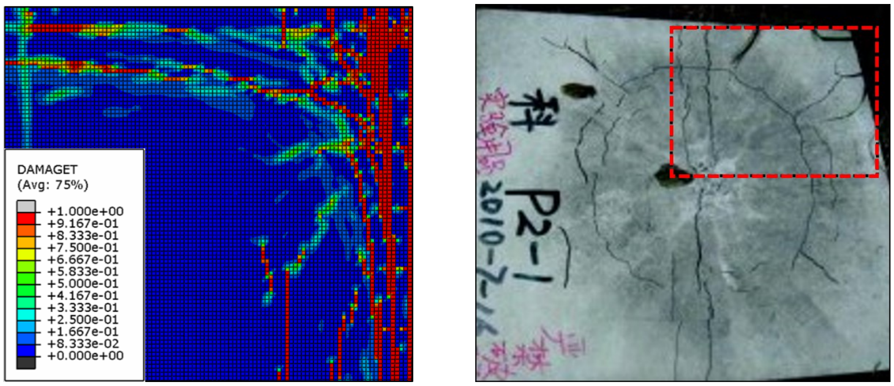

(a) 1/4-model in ABAQUS (b) Experiment

Figure A.15: Qualitative comparison between experimental results [20] and a 1/4-model in ABAQUS for the blast-receiving face of a reinforced concrete panel subjected to 0.31 kg of TNT at a stand-off of 0.4 m. Plotting contours of tensile damage parameter, d_t where $0 \leq d_t \leq 1$. Blue contours indicate $d_t = 0$ and red indicate $d_t > 0.9$. Image taken at step time = 0.02 s, well after maximum displacement is reached. Image (b) is reproduced from [20].

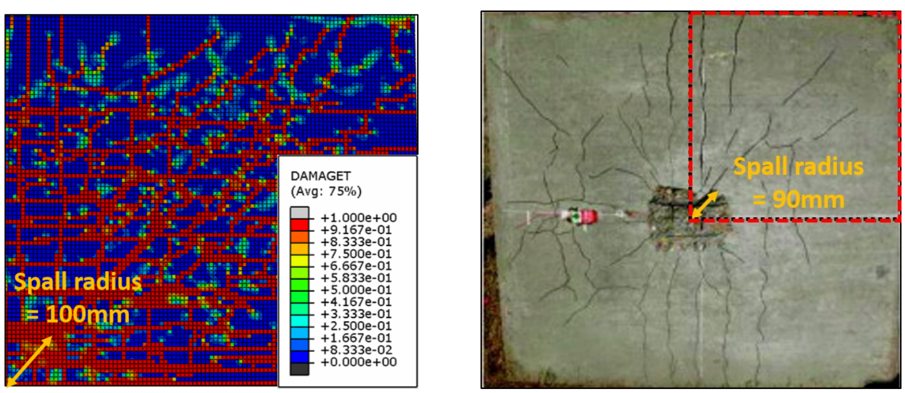

(a) 1/4-model in ABAQUS (b) Experiment

Figure A.16: Qualitative comparison between experimental results [20] and a 1/4-model in ABAQUS for the non-blast-receiving face of a reinforced concrete panel subjected to 0.31 kg of TNT at a stand-off of 0.4 m. Plotting contours of tensile damage parameter, d_t where $0 \leq d_t \leq 1$. Blue contours indicate $d_t = 0$ and red indicate $d_t > 0.9$. Image taken at step time = 0.02 s, well after maximum displacement is reached. Image (b) is reproduced from [20].

Quantitatively, comparison of slab deflections in Table A.4 show that predictions are acceptable within the limitations described above. The largest discrepancy is observed for a close-in blast case (0.31 kg of TNT at 0.4 m) and this discrepancy may be attributable as much to simplifications in the CONWEP load case as to the assumed constitutive model. Hence, we believe the CDP model is adequate for the purposes of this investigation.

Table A.4: Comparison between the maximum central slab deflection, δ_{max} predicted using the ABAQUS/Explicit numerical model with that obtained in literature experiments performed by Wang *et al.* (Case A) [20] and Wu *et al.* (Case B) [21].

Case	kg of TNT	Stand-off (m)	Experiment δ_{max} (mm)	ABAQUS δ_{max} (mm)
A	0.31	0.4	15	35
A	0.46	0.4	35	43
B	1	3	1.5	1.3
B	8.1	3	11	15

Appendix A.3. Elastomer

The elastomer is modelled using a hyperelastic relationship with a Yeoh strain energy potential as defined in [11]:

$$U = C_{10}(\bar{I}_1 - 3) + C_{20}(\bar{I}_1 - 3)^2 + C_{30}(\bar{I}_1 - 3)^3 + \frac{1}{D_1}(J^{el} - 1)^2 + \frac{1}{D_2}(J^{el} - 1)^4 + \frac{1}{D_3}(J^{el} - 1)^6 \quad \text{(A.10)}$$

where U is the strain energy per unit reference volume, C_{i0} and D_i are temperature-dependent material parameters and $\bar{I}_1$ is the first deviatoric strain invariant given by, $\bar{I}_1 = \bar{\lambda}_1^2 + \bar{\lambda}_2^2 + \bar{\lambda}_3^2$. $\bar{\lambda}_i$ are the deviatoric stretches defined as $\bar{\lambda}_i = J^{-\frac{1}{3}}\lambda_i$ where J is the total volume ratio and λ_i are the principal stretches. J^{el} is the elastic volume ratio given by $J^{el} = J/J^{th}$ where $J^{th} = (1 + \epsilon^{th})^3$ and ϵ^{th} is the linear thermal expansion strain obtained from the temperature and thermal expansion coefficient [11].

In conjunction, viscoelastic effects are accounted for using a Prony series. The Prony series parameters (non-dimensional shear relaxation modulus $\overline{g_n}$ and corresponding time constants, τ_n) were obtained from a literature source for a similar material [24] and are tabulated in Table A.5.

Table A.5: Prony series parameters, obtained from [24] and defined in [11].

n	$\overline{g_n}$	$\tau_n(s)$
1	0.94159	1.49E-6
2	1.31E-2	2.93E-5
3	1.01E-2	2.79E-4
4	7.62E-3	3.02E-3
5	5.69E-3	3.77E-2
6	4.17E-3	0.55586
7	3.01E-3	10.035
8	2.13E-3	236.29
9	1.43E-3	7521

Appendix B. 1D Coupled Eulerian-Lagrangian model validation

With reference to Fig. 5, an air column with dimensions $L = 6\,\mathrm{m}$ and $w_p = 0.01\,\mathrm{m}$ was modelled in Abaqus/Explicit as an Eulerian part with boundary conditions prescribed to ensure a 1D plane strain analysis throughout. A free-standing, rigid plate of dimensions $h_p = 0.1\,\mathrm{m}$, $w_p = 0.01\,\mathrm{m}$ was modelled as a discrete rigid part and assembled at a distance, $L_t = 3\,\mathrm{m}$ away from the inflow of the air column. The dimensions were chosen to minimise secondary wave reflections disrupting impulse transmission to the plate.

The air material model is based on the assumption that air can be treated as an ideal gas [26]. Table B.6 summarises the material model parameters, where, ρ_0 is the initial air density, p_0 is atmospheric pressure, R is the specific gas constant for dry air and c_v is the specific heat capacity at constant volume.

Table B.6: The user-defined parameters required to define the Eulerian air domain.

ρ_0 ($\mathrm{kg\,m^{-3}}$)	Temperature (K)	R ($\mathrm{J\,kg^{-1}K^{-1}}$)	p_0 (Pa)	c_v ($\mathrm{J\,kg^{-1}K^{-1}}$)
1.225	290	287	101,957	717.6

As a shock wave propagates in the non-acoustic regime, the wave shape changes. For the CEL model developed in this study, the distance between the inflow of the Eulerian domain and the target is kept as large as possible to avoid secondary wave reflections, as described above. Thus, the wave propagates a large distance before it interacts with the target structure and in turn, the wave shape distorts. An iterative procedure is required to determine the inflow boundary condition required to achieve the desired *free-field* wave profile at the target location.

The blast intensity chosen in this investigation was selected to be consistent with Kambouchev *et al.*'s intermediate blast intensity case [1] corresponding to $p_s/p_0 = 3.29$ and $I_i = 653\,\mathrm{Pa\,s}$. These are the incident, free-field loading parameters that we aim to achieve in the air column at point B in Fig. 5. An iterative procedure is performed to determine the velocity-time history necessary at point A, to achieve the desired pressure-time history at point B. A velocity boundary condition is prescribed as it has been shown to provide better modelling stability [27]. Equation B.1 presents this iterative calculation, where p_B is the measured free-field overpressure at point B, a_0 is the speed of sound and $u_{A[0]}$ is the particle velocity corresponding to the desired free-field overpressure at point B. The calculation proceeds until reasonable agreement is attained with the desired peak overpressure at point B. The incident impulse is checked against the desired value and the decay time, t_i may need to be adjusted. The iterative process then begins again.

$$u_{A[i+1]} = u_{A[i]} + \left(u_{A[0]} - a_0 \frac{5}{7} \frac{p_B}{p_0} \frac{1}{\sqrt{\frac{6}{7}\left(\frac{p_B}{p_0}\right) + 1}} \right) \tag{B.1}$$

For this case, the chosen inflow velocity boundary condition is given by; $u_A(t) = 701e^{-t/0.9\times10^{-3}}$ m/s. This generates a free-field peak overpressure at point B of $341\,\mathrm{kPa}$ ($p_s/p_0 = 3.34$) and an incident impulse of $698\,\mathrm{Pa\,s}$.

A number of simulations were performed to investigate how the relative transmitted impulse varies with Kambouchev *et al.*'s non-dimensional FSI parameter, β_s [1]. With reference to Eq. 4, different values of β_s were achieved by only varying the density of the rigid part, ρ_p between simulations. The blast intensity was kept constant as well as the plate depth, thereby fixing the values of t_i, ρ_s, U_s and h_p. The comparison between Kambouchev *et al.*'s expression (Eq. 3) [1] and that predicted by our numerical model is presented in Fig. B.17.

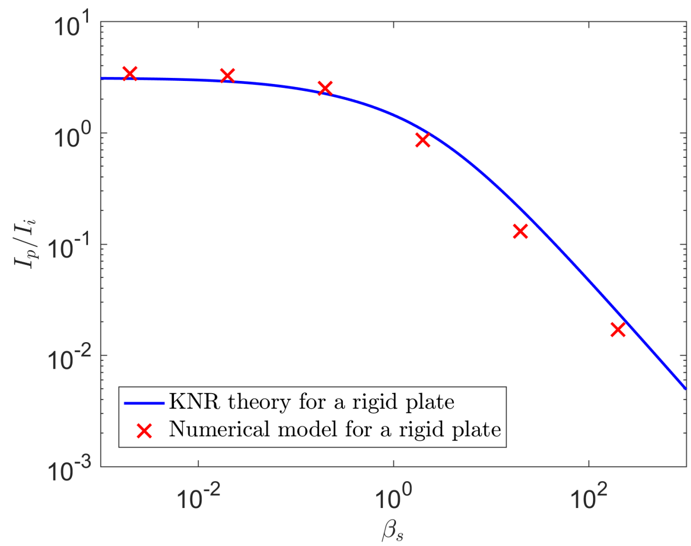

Figure B.17: A log-log plot of Kambouchev *et al.*'s (KNR) expression (Eq. 3) [1] for a rigid plate subjected to a blast intensity corresponding to $p_s/p_0 = 3.34$. The plot compares results obtained using our 1D CEL numerical model.

It should be noted that our numerical simulations modelled a rigid plate in the middle of an air column *i.e.* there was air on the front and back faces of the plate as illustrated in Fig. 5. This is not exactly the case considered by Kambouchev *et al.* [1]. Rather, their analysis was for a plate with no fluid on its back face (though a constant atmospheric pressure was applied to ensure the plate was initially in equilibrium). The close agreement between our simulations and Kambouchev *et al.*'s theory would suggest however, that the presence of air on the back face of the plate does not have a significant effect.

[1] Kambouchev N., Noels L., Radovitzky R., Nonlinear compressibility effects in fluid-structure interaction and their applications on the air-blast loading of structures, *Journal of Applied Physics*, Volume 100, 2006

[2] Davidson J. S., Porter, J. R., Dinan, R. J., Hammons, M. I., Connell J. D., Explosive testing of polymer retrofit masonry walls, *Journal of Performance of Constructed Facilities*, 2004, 18:2(100), 100-106

[3] Baylot J.T., Bullock B., Slawson T.R., Woodson S.C., Blast Response of Lightly Attached

Concrete Masonry Unit Walls, *ASCE Journal of Structural Engineering*, 2005, 131(8), 1186-1193

[4] Amini M.R., Isaacs J.B., Nemat-Nasser S., Investigation of effect of polyurea on response of steel plates to impulsive loads in direct pressure-pulse experiments, *Mechanics of Materials*, Volume 42, Issue 6, June 2010, 628-639

[5] Amini M.R., Simon J., Nemat-Nasser S., Numerical modeling of effect of polyurea on response of steel plates to impulsive loads in direct pressure-pulse experiments, *Mechanics of Materials*, Volume 42, 2010, 615-627

[6] Chen C.C., Alpman E., Linzell D.G., Long L.N., Effectiveness of advanced coating systems for mitigating blast effects on steel components, *Proceedings of the Tenth International Conference on Structures under Shock and Impact*, 14-16 May 2008, Algarve, Portugal

[7] Raman S.N., Ngo T., Mendis P., Pham T., Elastomeric Polymers for Retrofitting of Reinforced Concrete Structures against the Explosive Effects of Blast, *Advances in Materials Science and Engineering*, Volume 2012, Article ID 754142

[8] Xue Z. and Hutchinson J.W., A comparative study of impulse-resistant metal sandwich plates, *International Journal of Impact Engineering*, 2004, 30:1283-1305

[9] Fleck N.A. and Deshpande V.S., The resistance of clamped sandwich beams to shock loading, *Journal of Applied Mechanics*, 2004, 71:386-401

[10] Taylor G.I., The pressure and impulse of submarine explosion waves on plates. Batchelor G.K. editor, *The scientific papers of Sir Geoffrey Ingram Taylor, volume III: Aerodynamics and the Mechanics of Projectiles and Explosions*, Cambridge University Press, 1963, 287-303

[11] ABAQUS 2011, ABAQUS 6.11 *Analysis User's Manual*, Dassault Systemes, Providence, RI, USA

[12] CEBFIP, *CEB-FIP model code 1990: design code*, 1993, Thomas Telford

[13] An F., *Modelling of FRP-concrete interfacial bond behavior*, PhD Thesis, 2015, University of Edinburgh

[14] Hordijk D. A., *Local approach to fatigue of concrete*, PhD Thesis 1991, Delft University of Technology, Delft

[15] Birtel V. and Mark P., Parameterised finite element modelling of RC beam shear failure, *ABAQUS User's Conference*, 2006, Taiwan

[16] Lubliner J., Oliver J., Oller S., Onate E., A plastic-damage model for concrete, *International Journal of Solids and Structures*, Volume 25, 1989, 229-329

[17] Lee J. and Fenves G.L., A plastic-damage model for cyclic loading of concrete structures, *Journal of Engineering Mechanics*, Volume 124, No. 8, 1998, 892-90

[18] Hillerborg A., Modeer M., Petersson P.E., Analysis of crack formation and crack growth in concrete by means of fracture mechanics and finite elements, *Cement and Concrete Research*, Volume 6, 1976, 773-782

[19] ABAQUS 2011, ABAQUS 6.12 *Example Problems Manual, Volume 1: Static and Dynamic Analyses*, Dassault Systemes, Providence, RI, USA

[20] Wang W., Zhang D., Lu F., Wang S., Tang F., Experimental study and numerical simulation of the damage mode of a square reinforced concrete slab under close-in explosion, *Engineering Failure Analysis*, Volume 27, 2013, 41-51

[21] Wu C., Oehlers D.J., Rebentrost M., Leach J., Whittaker A.S., Blast testing of ultra-high performance fibre and FRP-retrofitted concrete slabs, *Engineering Structures*, Volume 31, 2009, 2060-2069

[22] Hyde D.W., Fundamentals of Protective Design for Conventional Weapons; CONWEP (Conventional Weapons Effects), United States Department of the Army: Washington, DC, USA, 1992

[23] ASTM D1822-13 Standard Test Method for Tensile-Impact Energy to Break Plastics and Electrical Insulating Materials, ASTM International, West Conshohocken, PA, 2013

[24] Mauchien T.K., *A fracture mechanics approach to accelerated life testing for cathodic delamination at polymer/metal interfaces*, Master of Science in Engineering thesis, University of Texas at Austin, May 2013

[25] Ngo T., Mendis P., Gupta A., Ramsay J., Blast loading and blast effects on structures — an overview, *EJSE Special Issue: Loading on Structures*, 2007

[26] Needham C.E., *Blast Waves*, Shock wave and high pressure phenomena, Springer-Verlag Berlin Heidelberg, 2010

[27] Mougeotte C., Carlucci P., Recchia S., Ji H., Novel approach to conducting blast load analyses using ABAQUS/Explicit-CEL, *Proceedings of 2010 Simulia Customer Conference*, Providence, Rhode Island (2007), p. 15

[28] Chen A., Louca L.A., Elghazouli A.Y., Behaviour of cylindrical steel drums under blast loading conditions, *International Journal of Impact Engineering*, Volume 88, 2016, 39-53

[29] Kinney G.F. and Graham K.J., *Explosive Shocks in Air*, Springer-Verlag, New York, NY, second edition, 1985

[30] Bomb threat stand-off distance chart, US National Counterterrorism Centre (NCTC), `https://www.dni.gov/files/NCTC/documents/features_documents/2006_calendar_bomb_stand_chart.pdf`

[31] Xue Z, Hutchinson JW. Preliminary assessment of sandwich plates subject to blast loads. *Int J Mech Sci*, 2003;45(4):687-705